Modulation of mechanical resonance by chemical potential oscillation in graphene

Changyao Chen[1†], Vikram V. Deshpande[2], Mikito Koshino[3], Sunwoo Lee[4], Alexander Gondarenko[1], Allan H. MacDonald[5], Philip Kim[6] and James Hone[1*]

The classical picture of the force on a capacitor assumes a large density of electronic states, such that the electrochemical potential of charges added to the capacitor is given by the external electrostatic potential and the capacitance is determined purely by geometry[1]. Here we consider capacitively driven motion of a nano-mechanical resonator with a low density of states, in which these assumptions can break down[2-5]. We find three leading-order corrections to the classical picture: the first of which is a modulation in the static force due to variation in the internal chemical potential; the second and third are changes in the static force and dynamic spring constant due to the rate of change of chemical potential, expressed as the quantum (density of states) capacitance[6,7]. As a demonstration, we study capacitively driven graphene mechanical resonators, where the chemical potential is modulated independently of the gate voltage using an applied magnetic field to manipulate the energy of electrons residing in discrete Landau levels[8-10]. In these devices, we observe large periodic frequency shifts consistent with the three corrections to the classical picture. In devices with extremely low strain and disorder, the first correction term dominates and the resonant frequency closely follows the chemical potential. The theoretical model fits the data with only one adjustable parameter representing disorder-broadening of the Landau levels. The underlying electromechanical coupling mechanism is not limited by the particular choice of material, geometry, or mechanism for variation in the chemical potential, and can thus be extended to other low-dimensional systems.

The calculation of the force between plates of a parallel-plate capacitor by energy methods is a classic problem that illustrates the importance of the correct definition of the system's free energy: considering only the energy stored in the capacitor incorrectly predicts a repulsive force of $(1/2)(\mathrm{d}C/\mathrm{d}z)\phi^2$, where C is the capacitance, $\mathrm{d}C/\mathrm{d}z$ is its spatial derivative, and ϕ is the electrostatic potential difference. The correct result (an attractive force $-(1/2)(\mathrm{d}C/\mathrm{d}z)\phi^2$) is obtained only when the work done by the battery to maintain a constant voltage is taken into account[1]. This result assumes a simple system of metallic capacitors with a large density of states (DOS), such that the chemical potential μ is constant and the electrostatic potential is identical to the voltage applied by the battery. This assumption breaks down in nanoscale systems, in which the DOS can be much smaller and μ is no longer fixed, an effect widely studied in electronic devices[6,7,11-14]. However, the role of a finite DOS in the force between capacitor plates has not been rigorously

investigated. Understanding the corrections to the classical model is of fundamental interest and important for modelling of nano-mechanical systems in the atomically thin limit[3,4]. Here we examine the case of a resonant nano-mechanical device, and show that the first-order correction to the resonant frequency consists of three terms: one term proportional to μ and the other two proportional to its derivative $\mathrm{d}\mu/\mathrm{d}n$, with the latter represented through the inverse quantum capacitance $C_Q^{-1} = (1/Ae^2)(\mathrm{d}\mu/\mathrm{d}n)$ (A is the sample size and e is the electron charge). The phenomenon is explored experimentally by examining the behaviour of a graphene resonator, in which μ is tuned by a perpendicular magnetic field B at a fixed electrochemical potential. We observe strong frequency shifts, which are periodic in $1/B$, and can be quantitatively described by the theoretical model. We further find that, in the limit of an ultra-clean device with low tension, the first term can provide the dominant tuning effect, demonstrating that a nano-mechanical device can be used to track its own chemical potential.

We model a generic mechanical resonator as a mass on a nonlinear spring, capacitively actuated by a nearby gate electrode, as shown in Fig. 1. A direct current (d.c.) voltage V_g applied to the gate can both increase the resonant frequency by exerting a static force to change the equilibrium deflection z_e, and decrease the frequency owing to the nonlinear electrostatic potential, an effect known as electrostatic spring softening[15]. The two effects provide an effective spring constant given by:

$$k_{\mathrm{eff}} = k + \eta \alpha z_e^2 - \frac{1}{2}\frac{\mathrm{d}^2 C_{\mathrm{total}}}{\mathrm{d}z^2}V_g^2 \qquad (1)$$

where k is the linear spring constant, α is the elastic nonlinear coefficient, and η is the geometric coefficient, which depends on the exact form of static deflection (see Supplementary Section 2). In rigid microelectromechanical devices (MEMS), the last (capacitive softening) term provides the dominant tuning effect, whereas in atomically thin materials under low tension, the second (mechanical stiffening) term can dominate.

The role of the finite density of states is modelled by considering the variation in μ with carrier density n, such that the electrostatic potential is given by $\phi = V_g - \mu/e$, and by including C_Q in series with C_g. In this case, we first find that the static capacitive force is given by (Supplementary Section 3):

$$F = -\frac{1}{2}\left(V_g - \frac{\mu}{e}\right)^2\left(1 - 2\frac{C_g}{C_Q}\right)\frac{\mathrm{d}C_g}{\mathrm{d}z} \qquad (2)$$

[1]Department of Mechanical Engineering, Columbia University, New York, New York 10027, USA. [2]Department of Physics and Astronomy, University of Utah, Salt Lake City, Utah 84112, USA. [3]Department of Physics, Tohoku University, Sendai 980-8578, Japan. [4]Department of Electrical Engineering, Columbia University, New York, New York 10027, USA. [5]Department of Physics, University of Texas, Austin, Texas 78712, USA. [6]Department of Physics, Harvard University, Cambridge, Massachusetts 02138, USA. [†]Present address: Center for Nanoscale Materials, Argonne National Laboratory, Lemont, Illinois 60439, USA. *e-mail: jh2228@columbia.edu
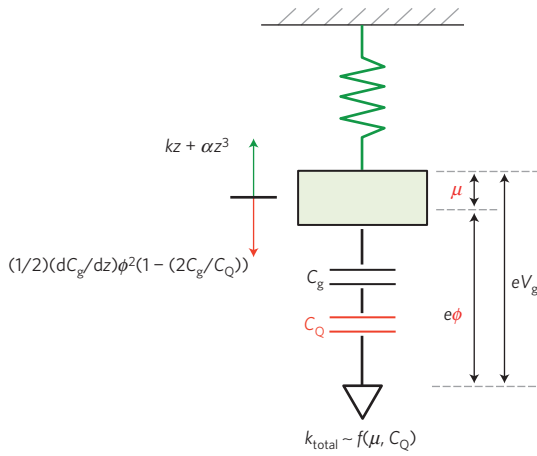
Figure 1 | Mass on a nonlinear spring balanced with electrostatic force.
The force exerted by the spring varies nonlinearly with the displacement z, and the electrostatic force is determined not only by the gate capacitance C_g and the electrostatic potential ϕ, but also by the quantum capacitance C_Q. For fixed electrochemical potential V_g, ϕ is directly modified by the chemical potential μ, therefore the total spring constant k_{total} is modulated by both μ and C_Q, and magnified by the nonlinear effect (large α).

When V_g is kept constant and μ and C_Q are modulated, the change in static force is approximated as:

$$\Delta F \approx - \left[\frac{\Delta \mu}{e} + C_g V_g \Delta \left(\frac{1}{C_Q} \right) \right] V_g \frac{dC_g}{dz} \quad (3)$$

The change in static force shifts the equilibrium deflection z_e—and thus the resonant frequency—and alters the curvature of the potential energy at the equilibrium position, as determined from the spatial derivative of ΔF. The leading term in the latter is given by:

$$\Delta k = \frac{d\Delta F}{dz} = \left(V_g \frac{dC_g}{dz} \right)^2 \Delta \left(\frac{1}{C_Q} \right) \quad (4)$$

Combining the effects from equations (2) and (3), we arrive at the total frequency shift as:

$$\Delta f_{total} = -\Re_V \left(\frac{\Delta \mu}{e} \right) - \Re_V C_g V_g \Delta \left(\frac{1}{C_Q} \right) \quad (5)$$
$$+ \frac{f_0}{2k_0} \left(V_g \frac{dC_g}{dz} \right)^2 \Delta \left(\frac{1}{C_Q} \right)$$

where $\Re_V = |df_0/dV_g|$ indicates how easily the resonant frequency f_0 can be tuned by electrostatic potential, k_0 is the unmodulated spring constant, $\Delta \mu$ is the change in the chemical potential, and $\Delta(1/C_Q)$ represents the change in the inverse quantum capacitance. The three terms in equation (5) are referred to below as Δf_1, Δf_2 and Δf_3, respectively. Importantly Δf_1 is a direct measure of variation in the chemical potential, whereas Δf_2 and Δf_3 depend on the change in quantum capacitance. We also note that these terms are closely related to experiments with nanotube quantum dot mechanical resonators[3,4], in which $\Delta f_{2,3}$ are analogous to the diverging charge susceptibility of the quantum dot that produces dips in the nanotube mechanical frequency at charge transitions, and Δf_1 plays a similar role that changes the static tension and the mechanical frequency from discretely charging the quantum dot.

We examine this phenomenon experimentally using graphene mechanical resonators[16,17], where a transverse magnetic field B is used to tune μ and C_Q independently of V_g. The samples are in a three-terminal configuration (Fig. 2a) with a local gate (LG) placed few hundred nanometres away from the suspended graphene. The graphene is assumed to have built-in strain ε_0 from the fabrication process, with additional strain induced by the d.c. gate voltage V_g. We use a continuum mechanical model for the calculation of $f(V_g)$ at different levels of ε_0 (Fig. 2b, also Supplementary Section 3). Figure 2c shows $\Re_V$ as a function of ε_0, at three different values of V_g, for a 2 by 2 μm single-layer graphene resonator. Thus, in devices with low ε_0, $\Re_V$ can be large and $\Delta f_{1,2}$ are maximized, whereas in devices with large ε_0, $\Re_V$ is substantially smaller and $\Delta f_{1,2}$ should be minimized relative to Δf_3. We note that previous studies of graphene resonators in high magnetic fields[5] utilized samples with high tension and, therefore, observed only the effects of Δf_3; in the experimental work below, we focus on samples with ultralow tension to directly observe the effects of chemical potential variation.

In a transverse magnetic field, electronic states of graphene form discrete Landau levels (LLs), and μ oscillates in a sawtooth pattern with increasing B. The oscillation in μ is reflected in the longitudinal electrical resistivity[8–10] (Shubnikov–de Haas oscillations), and in the magnetization $M = -d\mu/dB$ (de Haas–van Alphen oscillations, typically detected by torque magnetometry[2]), but can also be studied explicitly using a sensitive single-electron transistor electrometer[18,19]. In a single-particle picture, the dependence of μ and C_Q on B is determined by the filling fraction $\nu = 2\pi n\hbar/eB$ ($\hbar$ is the reduced Planck's constant) and disorder. We construct a simple model[20] consisting of up to 20 Gaussian-broadened LLs with disorder-induced width Γ (in units of $\nu_F \sqrt{2e\hbar B}$, where $\nu_F = 10^6$ m s^{-1} is the Fermi velocity). The DOS is given by $D(E) = dn/d\mu \propto \sum^N \exp[-(E - E_N)^2/\Gamma^2]$, where E_N is the centre of the Nth LL. Within each LL, E_N of single-layer graphene evolves with B as $E_N(B) = \nu_F \text{sgn}(N)\sqrt{2e\hbar B|N|}$. Here μ is assigned as the highest filled energy level, and C_Q is defined as $Ae^2 D(E)$, where A is the sample area. Figure 2d–f shows the simulated $\Delta \mu$ as a function of B and accompanying frequency shifts calculated from each of the terms in equation (5) for three different combinations of high/low tension and disorder. In the case of low tension but large disorder (Fig. 2d), $\Delta f_{1,2,3}$ are all reflected in the total frequency shift, but LL broadening largely obscures the variation in μ. In the case of high tension and small disorder (Fig. 2e), we found that $\Delta f_3 > \Delta f_{1,2}$ as expected, leading to sharp spikes in frequency at LL transitions. Finally, in the case of both low tension and low disorder (Fig. 2f), the frequency shift closely (but not completely) follows the contribution of Δf_1 and the sawtooth variation of μ, with spikes at the transitions between LLs due to $\Delta f_{2,3}$.

This simulation motivates the use of graphene samples with very low built-in strain and disorder, to directly observe variation in μ. To prevent contamination, we prepare samples by direct exfoliation of graphite over pre-patterned electrodes[21], and further clean the graphene by Joule heating in vacuum at low temperature[22,23]. The electronic quality is examined through separate measurements (Supplementary Section 1), and can yield a charged impurity density as low as $\sim 8 \times 10^9$ cm^{-2}. For mechanical resonance measurements, the graphene is actuated electrostatically by adding a small radiofrequency drive voltage to the gate, and the gate–drain current at the same frequency is read out by a vector network analyser; on resonance, the changing capacitance due to mechanical motion causes a measurable peak in the current[21,24]. The absence of d.c. bias avoids Joule heating and possible Lorentz forces. We scan V_g up to ± 10 V at zero magnetic field to determine $\Re_V$ and use the continuum mechanical model to extract ε_0. The use of substrate-fixed electrodes eliminates tensioning owing to thermal contraction of the metal[17,25], and we are able to achieve $\Re_V$ as large as 10 MHz V^{-1}, with $\varepsilon_0 \sim 10^{-4}$.

Figure 3a shows the response of the mechanical resonance to the applied magnetic field B, for device D1 with $\Re_V$ of 2 MHz V^{-1}.
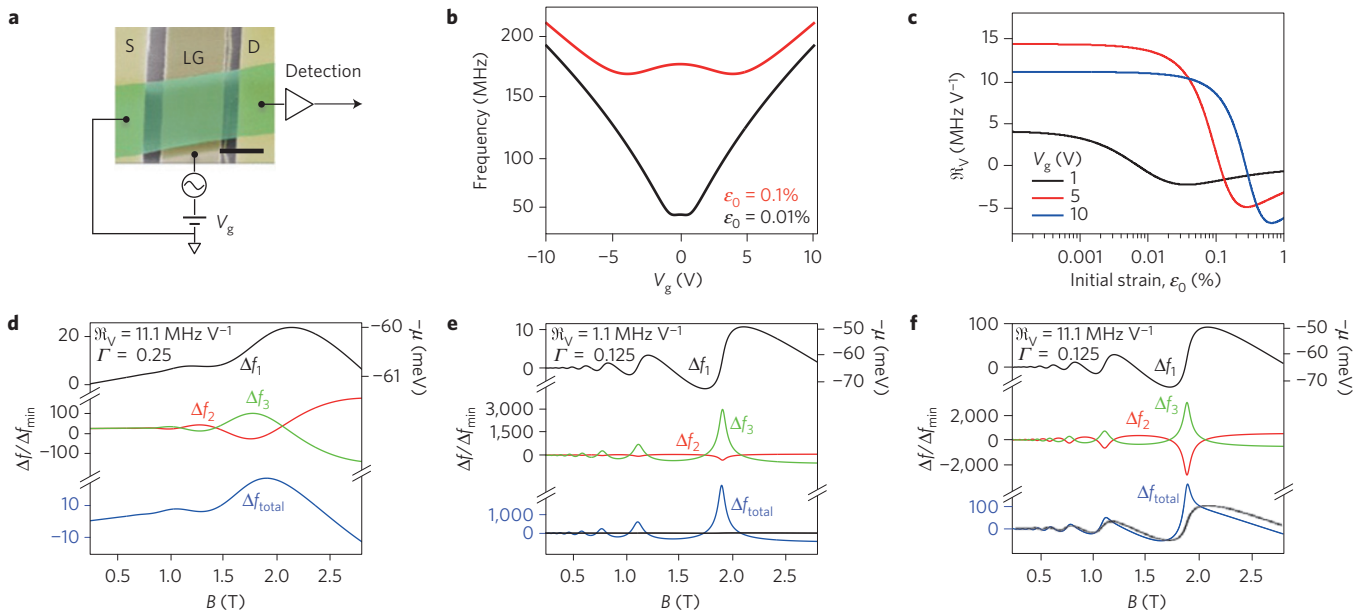
Figure 2 | Mechanical resonance modulation. a, Schematic of the graphene mechanical resonator with source (S), drain (D) and local gate (LG) contacts. Scale bar, 1 μm. **b,** Simulated resonant frequency for a 2 by 2 μm graphene resonator with a 120 nm gap, at different initial strain ε_0. **c,** Calculated $\Re_V$ as a function of initial strain ε_0 for a single-layer graphene resonator, at different gate voltage V_g. The negative $\Re_V$ indicates an electrostatic softening effect. **d–f,** Simulated frequency shifts under high disorder and large $\Re_V$, (**d**); low disorder and small $\Re_V$ (**e**); low disorder and large $\Re_V$ (**f**). Top panel: μ (to the right) and corresponding frequency oscillation Δf_1 (to the left) as a function of magnetic field B. Middle panel: corresponding frequency shifts Δf_2 and Δf_3 (see main text). Bottom panel: the total frequency shift as function of B, with Δf_1 overlaid on top (black), except for **d**. For all the simulations, $V_g = 10$ V, $\varepsilon_0 = 0.01\%$, $Q = 2,000$, signal-to-noise ratio = 10 dB, $f_0 = 161.4$ MHz, and f_{min} is 360 Hz assuming a 100 Hz measurement bandwidth.

There is no obvious frequency shift with B, except for regimes between LLs, where sharp spikes are evident but the signal becomes weak. Such observations agree well with the predictions for small $\Re_V$ and experimental results reported by Singh and colleagues. Figure 3b shows the same measurements on device D2 (length 2.4 μm, width 3.2 μm), with $\Re_V$ of 10 MHz V^{-1}. The data reveal a repeated pattern of oscillations that are periodic in $1/B$ (Supplementary Section 4), allowing us to directly extract the carrier density n of 2.4×10^{11} cm^{-2}. We use the measured values of n at five values of V_g to obtain C_g. Finite element simulation (COMSOL Multiphysics) is then used to obtain the effective displacement z_e, and dC_g/dz_e is approximated as C_g/z_e. Therefore, the only free parameter left to fit equation (5) is the disorder level Γ, which will determine $\Delta\mu$ and $\Delta(1/C_Q)$. We found that a Γ of 0.1 gives a satisfactory result. The corresponding $\mu(B)$, that gives rise to Δf_1, is overlaid as a yellow curve in Fig. 3b. For comparison, we also plot $E_N(B)$ for the first five LLs as dotted green lines. We found that μ traces E_N closely in each LL, confirming that the frequency can closely track μ in high-quality samples. The detailed fit between the model and the data is shown in Fig. 3c. Here, the circles represent the resonant frequency extracted at each value of B from the data in Fig. 3b, and the line represents the prediction of equation (5) with $\Gamma = 0.1$. The fit is excellent and validates the model presented above.

We briefly consider the region between LLs, where the frequency shift should be primarily sensitive to C_Q. At high magnetic fields, when the sample enters the well-developed quantum Hall regime, its bulk becomes insulating and the edges host dissipationless one-dimensional edge states. This will not change the static charge on the sample and the static force due to V_g, and therefore first two terms of equation (5) should be unaffected. However, when the bulk becomes sufficiently insulating such that its RC charging time is greater than the mechanical resonance period, the dynamic charging should be determined by the geometric capacitance between the gate and the edge channels, which can be an order of magnitude smaller than C_g (see Supplementary Section 5). This has two consequences. First,

both the third term in equation (5) and the classical electrostatic softening term in equation (1) should decrease with the decreasing dynamic capacitance; in general, the classical term will dominate and the frequency spike will be larger than predicted by equation (5). Second, both the radiofrequency drive and capacitive displacement current will also decrease, leading to substantial loss of signal. As a consequence, we can use the loss of signal to directly determine the onset of the bulk insulating behaviour. In Fig. 3b,c (also see Supplementary Fig. 11), this is seen to occur for the final spike, at the transition between $N = 2$ and $N = 1$, indicated by the dashed line in Fig. 3c. For this transition, we expect that the model will not fit the data well; indeed, the magnitude and width of the frequency spike, where observable, seem to exceed the prediction. Nevertheless, the best fit of the limited data in the region between LLs yields C_Q with values similar to previous measurements of high-quality graphene samples[26,27]. More detailed modelling and alternative transduction techniques (for example, optical detection) may allow better study of the detailed behaviour between LLs.

Figure 4a shows similar data at different values of V_g, with fits using Γ values within ±10%. Because we are able to 'read off' chemical potential variation directly through mechanical resonance shifts, we can then track the chemical potential as a function of the filling fraction ν. Figure 4b shows $\Delta\mu(\nu)$ at four different values of V_g: there are distinct jumps of μ at $\nu = 4(N + 1/2)$, which represent the energy gaps between neighbouring LLs. We linearly extrapolate to extract the energy gaps, as plotted in Fig. 4c. In addition, the same analysis allows extrapolation to determine the chemical potential at zero magnetic field $\mu_0 = \hbar v_F \sqrt{\pi n}$. As shown in Fig. 4d, this follows $\sqrt{V_g}$ as expected. Therefore, the mechanical measurements can, under appropriate conditions, provide a direct means to monitor the chemical potential evolution of the underlying system, in a straightforward manner. We expect to extend our measurements into extreme quantum regimes at larger B, where additional chemical potential jumps would suggest the formation of many-body incompressible states.
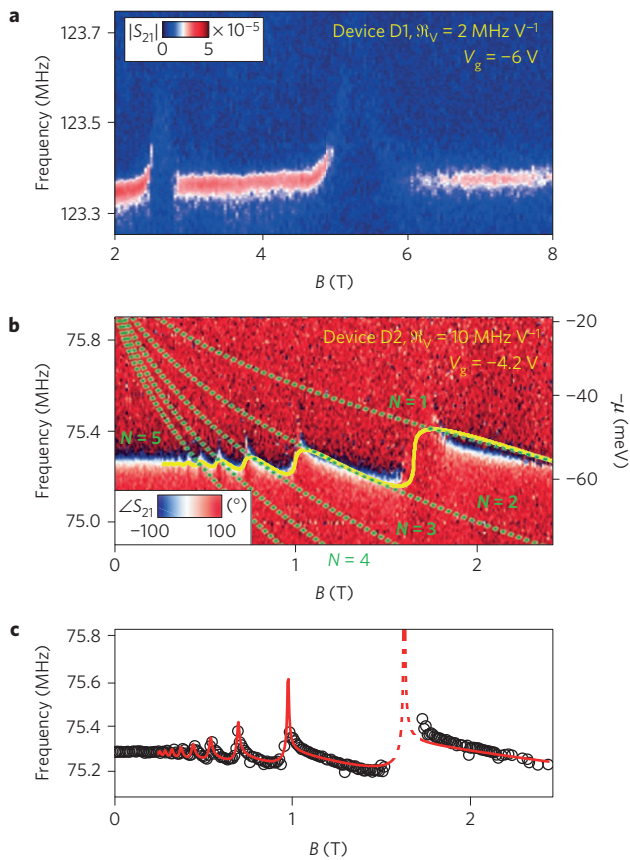
Figure 3 | Chemical-potential-variation-induced frequency shifts.
a, Measured magnitude of S_{21} transmission as a function of applied magnetic field for device D1. Owing to the small frequency tunability, there is no obvious mechanical resonance shift within a single LL. Test conditions: $T = 4.3$ K, $V_g = -6$ V, drive power is -62 dB m. **b**, Similar measurement for device D2, which has a greater frequency tunability. The corresponding chemical potential variation is overlaid in yellow. The green dotted lines show the LL energies for $N = 1$–5. Test conditions: $T = 4.3$ K, $V_g = -4.2$ V, drive power is -68 dB m. **c**, Complete fitted result (red curve) to the data shown in **b**. The dashed line indicates where the model is not expected to be accurate.

Our nano-mechanical technique thus provides access to a key thermodynamic quantity (chemical potential) in a self-contained manner. Specifically, our system allows measurements of both the energy gaps and the gradual energy transition between gaps, which would otherwise require specialized instrumentation[18,19]. In the future, measurements of other correlation effects such as negative compressibility[28,29], fractional quantum Hall effects[19,30–34] and Wigner crystallization[35], all of which have thermodynamic signatures, should be possible using this technique. Finally, we emphasize that the electromechanical mechanism identified in the present work is not specific to graphene. Indeed, any atomically thin mechanical resonator with a quasi-2D electronic structure will demonstrate this sensitive response to external fields via an electrostatically controlled mechanism.

Methods

Methods and any associated references are available in the online version of the paper.
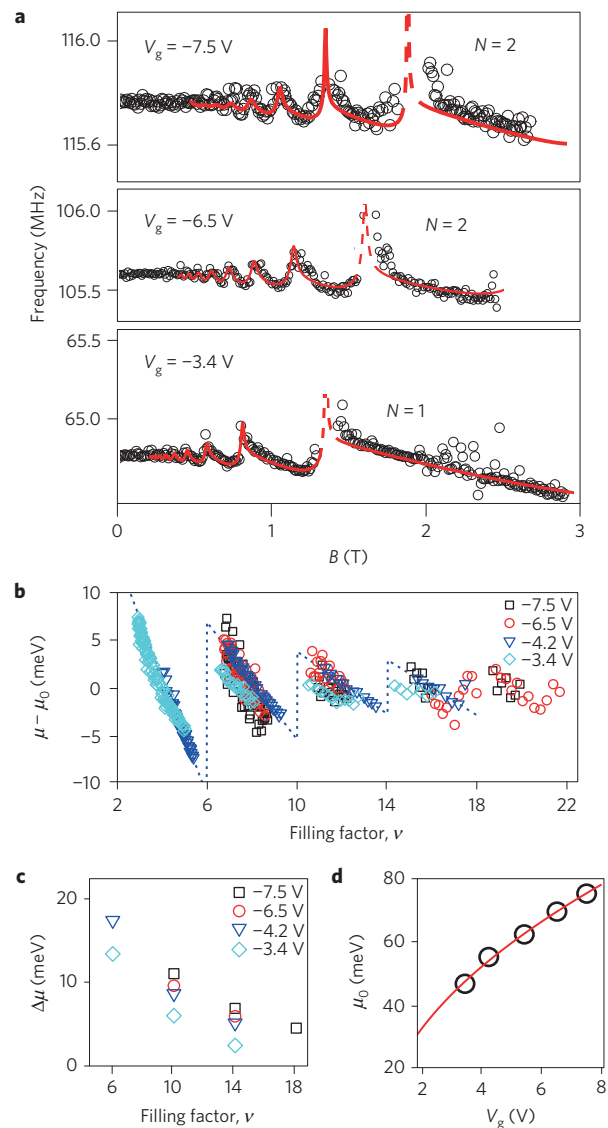
Figure 4 | Chemical potential evolutions and overall fits to experimental data. a, Mechanical resonant frequency as functions of the applied magnetic fields at different V_g, and corresponding fits (red curves). The dashed lines indicate where the model is not expected to be accurate (see text). **b**, Extracted chemical potential changes for different V_g, as a function of the filling factors. The dashed blue line shows the linear extrapolation used to determine the energy gaps at integer filling factors. **c**, Energy gaps at different integer filling factors for various V_g. **d**, Chemical potential at zero magnetic field, μ_0 at different V_g. Red solid curve is a $\sqrt{V_g}$ fit.

References

1. Feynman, R. P., Leighton, R. B. & Sands, M. *The Feynman Lectures on Physics* Vol. 2 (Basic Books, 2013).
2. Eisenstein, J. P. *et al.* Density of states and de Haas–van Alphen effect in two-dimensional electron systems. *Phys. Rev. Lett.* **55,** 875–878 (1985).
3. Steele, G. A. *et al.* Strong coupling between single-electron tunneling and nanomechanical motion. *Science* **325,** 1103–1107 (2009).
4. Lassagne, B., Tarakanov, Y., Kinaret, J., Garcia-Sanchez, D. & Bachtold, A. Coupling mechanics to charge transport in carbon nanotube mechanical resonators. *Science* **325,** 1107–1110 (2009).
5. Singh, V. *et al.* Coupling between quantum Hall state and electromechanics in suspended graphene resonator. *Appl. Phys. Lett.* **100,** 233103 (2012).
6. Ilani, S., Donev, L. A., Kindermann, M. & McEuen, P. L. Measurement of the quantum capacitance of interacting electrons in carbon nanotubes. *Nature Phys.* **2,** 687–691 (2006).

7. Xia, J., Chen, F., Li, J. & Tao, N. Measurement of the quantum capacitance of graphene. *Nature Nanotech.* **4,** 505–509 (2009).
8. Zhang, Y. B., Tan, Y. W., Stormer, H. L. & Kim, P. Experimental observation of the quantum Hall effect and Berry's phase in graphene. *Nature* **438,** 201–204 (2005).
9. Novoselov, K. S. *et al.* Two-dimensional gas of massless Dirac fermions in graphene. *Nature* **438,** 197–200 (2005).
10. Castro Neto, A. H., Guinea, F., Peres, N. M. R., Novoselov, K. S. & Geim, A. K. The electronic properties of graphene. *Rev. Mod. Phys.* **81,** 109–162 (2009).
11. Klitzing, K. v., Dorda, G. & Pepper, M. New method for high-accuracy determination of the fine-structure constant based on quantized Hall resistance. *Phys. Rev. Lett.* **45,** 494–497 (1980).
12. Fulton, T. A. & Dolan, G. J. Observation of single-electron charging effects in small tunnel junctions. *Phys. Rev. Lett.* **59,** 109–112 (1987).
13. Luryi, S. Quantum capacitance devices. *Appl. Phys. Lett.* **52,** 501–503 (1988).
14. Park, J. *et al.* Coulomb blockade and the Kondo effect in single-atom transistors. *Nature* **417,** 722–725 (2002).
15. Lifshitz, R. & Cross, M. C. in *Reviews of Nonlinear Dynamics and Complexity* Vol. 1 (ed. Schuster, H. G.) 1–52 (Wiley-VCH, 2009).
16. Bunch, J. S. *et al.* Electromechanical resonators from graphene sheets. *Science* **315,** 490–493 (2007).
17. Chen, C. *et al.* Performance of monolayer graphene nanomechanical resonators with electrical readout. *Nature Nanotech.* **4,** 861–867 (2009).
18. Zhitenev, N. B. *et al.* Imaging of localized electronic states in the quantum Hall regime. *Nature* **404,** 473–476 (2000).
19. Feldman, B. E., Krauss, B., Smet, J. H. & Yacoby, A. Unconventional sequence of fractional quantum Hall states in suspended graphene. *Science* **337,** 1196–1199 (2012).
20. Koshino, M. & Ando, T. Diamagnetism in disordered graphene. *Phys. Rev. B* **75,** 235333 (2007).
21. Xu, Y. *et al.* Radio frequency electrical transduction of graphene mechanical resonators. *Appl. Phys. Lett.* **97,** 243111 (2010).
22. Moser, J., Barreiro, A. & Bachtold, A. Current-induced cleaning of graphene. *Appl. Phys. Lett.* **91,** 163513 (2007).
23. Bolotin, K. *et al.* Ultrahigh electron mobility in suspended graphene. *Solid State Commun.* **146,** 351–355 (2008).
24. Chen, C. *Graphene NanoElectroMechanical Resonators and Oscillators* PhD thesis, Univ. Columbia (2013).
25. Singh, V. *et al.* Probing thermal expansion of graphene and modal dispersion at low-temperature using graphene nanoelectromechanical systems resonators. *Nanotechnology* **21,** 165204 (2010).
26. Martin, J. *et al.* The nature of localization in graphene under quantum Hall conditions. *Nature Phys.* **5,** 669–674 (2009).
27. Yu, G. *et al.* Interaction phenomena in graphene seen through quantum capacitance. *Proc. Natl Acad. Sci. USA* **110,** 3282–3286 (2013).
28. Efros, A. Density of states of 2d electron gas and width of the plateau of IQHE. *Solid State Commun.* **65,** 1281–1284 (1988).
29. Kravchenko, S. V., Rinberg, D. A., Semenchinsky, S. G. & Pudalov, V. M. Evidence for the influence of electron–electron interaction on the chemical potential of the two-dimensional electron gas. *Phys. Rev. B* **42,** 3741–3744 (1990).
30. Bolotin, K. I., Ghahari, F., Shulman, M. D., Stormer, H. L. & Kim, P. Observation of the fractional quantum Hall effect in graphene. *Nature* **462,** 196–199 (2009).
31. Du, X., Skachko, I., Duerr, F., Luican, A. & Andrei, E. Y. Fractional quantum Hall effect and insulating phase of Dirac electrons in graphene. *Nature* **462,** 192–195 (2009).
32. Dean, C. R. *et al.* Multicomponent fractional quantum Hall effect in graphene. *Nature Phys.* **7,** 693–696 (2011).
33. Dean, C. *et al.* Hofstadter's butterfly and the fractal quantum Hall effect in moire superlattices. *Nature* **497,** 598–602 (2013).
34. Ponomarenko, L. *et al.* Cloning of Dirac fermions in graphene superlattices. *Nature* **497,** 594–597 (2013).
35. MacDonald, A. H., Oji, H. C. A. & Liu, K. L. Thermodynamic properties of an interacting two-dimensional electron gas in a strong magnetic field. *Phys. Rev. B* **34,** 2681–2689 (1986).

Author contributions

C.C. and V.V.D. fabricated and characterized the samples, developed the measurement technique and performed the experiments, data analysis and theoretical modelling. M.K. performed disorder-broadened calculations. S.L. and A.G. helped in sample fabrication. A.H.M. provided theoretical support. P.K. and J.H. oversaw the project. C.C., V.V.D., P.K. and J.H. co-wrote the paper. All authors discussed and commented on the manuscript.

Additional information

Supplementary information is available in the online version of the paper. Reprints and permissions information is available online at www.nature.com/reprints. Correspondence and requests for materials should be addressed to J.H.

Competing financial interests

The authors declare no competing financial interests.

Methods

Device fabrication. High-resistivity silicon wafers ($>20{,}000\,\Omega\,cm$) are used in the experiments described in the main text, to minimize the parasitic capacitance in the radiofrequency (RF) range. 290 nm of thermal oxide is then grown to have the best optical contrast for identifying single-layer graphene in later studies.

Source and drain electrodes (1 nm Cr, 15 nm Au) are first patterned by deep ultraviolet photo-lithography (ASML 300C DUV stepper, Cornell Nanofabrication Facility). Next, a dry etch (CF_4) creates 200-nm-deep trenches between source and drain electrodes, and finally local gate electrodes (1 nm Cr, 20 nm Au) are deposited in the trenches with careful alignment. The details of the fabrication are described elsewhere[24].

Graphene samples are prepared by mechanical exfoliation of kish graphite. The colour contrast of the substrate-supported region aids in identification of thin flakes crossing the electrodes. The precise number of layers is subsequently confirmed by Raman spectroscopy.

Device characterization. Suspended graphene samples are electrically tested at room temperature under vacuum before cool-down. Only samples that possess reasonable transconductance ($\Delta R > 100\,\Omega$ within ±10 V change of gate voltage) are chosen for further investigation.

For low-temperature measurements in a magnetic field, samples are wire-bonded and loaded into an in-house-built insert for the Quantum Design physical properties measurement system (PPMS, 1.8 K base temperature) with eight semi-rigid coaxial cables to transmit both d.c. and RF signals. Most suspended graphene samples show improved quality (narrower Dirac peak) on cooling. Sample quality is further improved by gentle current annealing[23]. After such treatments, the smallest full-width at half-maximum (FWHM) of the Dirac peak is about 0.2 V, corresponding to a disorder density of $\sim 8 \times 10^9\,cm^{-2}$. To avoid the graphene collapsing as a result of electrostatic forces, we apply a gate voltage only within ±10 V.